Numerical simulations of the wake and deformations of a flexible rotor blade in a turbulent flow

Marwa Fakhfekh, Wael Ben Amira, Malek Abid, Aref Maalej

Numerical simulations of the wake and deformations of a flexible rotor blade in a turbulent flow

Marwa Fakhfekh,[1] Wael Ben Amira,[1,2] Malek Abid,[3] and Aref Maalej[1]
[1)]*Laboratory of Electromechanical Systems, National Engineering School of Sfax - University of Sfax, Soukra km 3.5, Sfax, 3038, Tunisia*
[2)]*Department of Mechanical Engineering, Higher Institute of Industrial Systems of Gabès - University of Gabès, Gabes, 6029, Tunisia*
[3)]*Aix-Marseille Université, Institut de Recherche sur les Phénomènes Hors Equilibre, UMR 7342, CNRS, Centrale Méditerranée, Marseille, 13384, France*

(*Electronic mail: aref.maalej@enis.tn)

(*Electronic mail: abid@irphe.univ-mrs.fr ; Corresponding author)

(*Electronic mail: benamira.wael@gmail.com)

(*Electronic mail: marwa.fakhfekh@enis.tn)

(Dated: 1 March 2024)

We present, for the first time, the mean deflection evolution of a flexible rotor blade using a coupled model based on Navier-Stokes equations, for the fluid flow, and linear elasticity equations for the blade deformation. Three turbulence models are tested to reach Reynolds numbers as high as $8\ 10^4$. The absolute tip speed ratios are in the range $[0, 25]$. The numerical results are validated by comparisons with available tip displacements from experiments. For the parameter ranges, above-mentioned, the elastic behavior of the flexible rotor is characterized, and the vorticity field is compared with results obtained for a rigid rotor. The effects of the pitch, the tip speed ratio (or frequency), and its sign, on the blade deformation are reported. Typically, the blade deforms in the downstream direction, and it is shown that this deformation is a non-monotonic function of the rotation frequency and the pitch angle. Furthermore, it is found that, for particular values of the frequency and pitch angle, the blade is subject to deformations in the upstream direction. It is shown also that the flexible rotor could develop a vortex ring state, but not the rigid one, under the same conditions. It is found that there is a supercritical frequency associated with the apparition of this vortex ring state and this frequency occurs for negative pitches only, for the considered blade. The vorticity field revealed, as well, that the tip vortex changes sign with that of the blade deflection. Finally, we present the effect of the pitch and frequency on the twist angle of the blade and characterize its evolution along the span.

I. INTRODUCTION

Rotors are often used in engineering applications, such as wind turbines, propellers and helicopters. Flexible rotor blades are a type of rotor blade used in wind turbines. They are designed to be able to bend and flex in order to reduce the effects of turbulence and other external forces on the turbine. This helps to increase the efficiency of the turbine and reduce the wear and tear on the blades. Flexible rotor blades are made from composite materials such as carbon fiber or fiberglass and are designed to be light and flexible. They are usually mounted on a central hub, which allows them to pivot and rotate in response to the wind. Generally, a flexible rotor blade is more efficient than a rigid blade because it is able to deform and adjust to the changing air flow, allowing it to generate more lift and reduce drag. Additionally, the flexibility of the blade can reduce vibration and noise, which can improve the overall performance of the rotor. Nowadays, there are several works, which are interested in improving the performance of wind turbines (vertical-axis wind turbine (VAWT) and horizontal-axis wind turbine(HAWT)), increasing their efficiency and their energy production. The main objectives of these works are to characterize the aerodynamic parameters and aspect of the blade[1], to study and characterize the wake and the stability of the flows behind the rotors[2], and to release the aerodynamic loads on the wind blades[3–5]. In these works, different experimental and computational approaches are used, like Vortex Method (VM)[6], Computational Fluid Dynamic(CFD)[7–10], Blade Element Momentum method (BEM)[11–13] and Fluid-Structure Interaction methods(FSI)[14–16]. However, in these studies, they are not interested in the deformation of the blades.

The need of wind power and energy have increased in the last decades. Then, the capacity and dimensions of wind turbine have also increased to meet this need and reduce the cost of wind power generation. The increasing size of large turbines can introduce aero elastic effects, and the blades can experience elastic deflections due to the aerodynamic loads[17]. On the one hand, the blade flexibility can harm the operation of the rotor because it can lead to excessive deformation of the blades and thus cause undesirable instabilities of the fluid-structure interaction[18,19]. On the other hand, the design of flexible rotor blades requires a good sizing of the elastic parameters to guarantee the resistance and to avoid the damage to the structure due to the aerodynamic forces. For these reasons, the aero elastic problem is the subject of various studies aimed at characterizing the effect of elasticity on the aerodynamic behavior of flexible bodies in flows, such as the work of Gosselin et al.[20,21]. They presented an experimental setup to study the effect of the flexibility and the reconfiguration on the drag reduction. Bano T. et al.[22] have analyzed the aerodynamic parameters of flexible flaps, fixed to the bottom and

placed normal to the flow. Chris Sungkyun Bang et al.[23] developed an FSI method to quantify the coupled effect of structural and aerodynamic performance of the front wing of a Formula One. However, these studies do not take into account the rotation of the bodies.
V. Rama Krishna et al.[24] presented a numerical study using the two-way-FSI analysis to predict the hydro-elastic response of a marine propeller. As a result, they predict the peak value of stress and deformation developed during the transient stage.
A.S. Eldemerdash and T. Leweke[25] developed an experimental investigation of fluid-structure interaction, of a flexible rotating rotor in water, to study the effect of hydrodynamic parameters on the elastic behavior of the blades. They presented the induced torsion and the flapwise bending deformation of the blade.
Due to the high cost of experimental investigations, the emphasis has been put on numerical methods. Furthermore, numerical methods can give access to fluid features that are difficult to measure in experiments, such as the vortex field. In this context, we present this numerical study, based on the strong fluid structure interaction method, to study the blade deformation. The aim of this work is to characterize and study the effect of aerodynamic parameters, such as the rotation frequencies and the pitch angle, on the flapwise deformation and the torsion of the blade. To better quantify the deformations, the rotor operates in water, where fluid forces are greater than in air and can generate much larger deformations.

The paper is organized as follows. Section 2 is devoted to governing equations. The numerical simulations and their details are presented in section 3. Results and discussions are given in section 4 and section 5 is devoted to conclusions.

II. GOVERNING EQUATIONS:

The fluid-structure interaction problems for viscous fluid flow and large structural displacements are governed by the complete Navier-Stokes equations and the linear equations of elasticity, which are represented by the following system:

$$\rho_f \frac{\partial \mathbf{u}_f}{\partial t} + \rho_f (\mathbf{u}_f \cdot \bigtriangledown)\mathbf{u}_f = - \bigtriangledown p + \mu_f \bigtriangledown \cdot (\bigtriangledown \mathbf{u}_f) + F_v \quad (1)$$

$$\bigtriangledown . \mathbf{u}_f = 0 \quad (2)$$

$$\rho_s \frac{\partial^2 \mathbf{u}_s}{\partial t^2} - \nabla \cdot \boldsymbol{\sigma}^{solid} = F_s \quad (3)$$

Where $\mathbf{u}_f$ is the incompressible fluid velocity field, $\mathbf{u}_s$ is the displacement of the solid blade, t is time, μ_f is the dynamic viscosity, F_v is the body force on the fluid, in this case gravitational acceleration times ρ_f, and F_s is the force per unit volume on the blade. ρ_f and ρ_s are the fluid's and solid's density, respectively.
The constitutive relation of Hooke's law, also called the relation of linear elasticity is used:

$$\boldsymbol{\sigma}^{solid} = 2\mu_s \boldsymbol{\epsilon} + \lambda_s tr(\boldsymbol{\epsilon})\mathbf{I} \quad (4)$$

$$\mu_s = \frac{E}{2(1+\upsilon)} \quad and \quad \lambda_s = \frac{E\upsilon}{(1+\upsilon)(1-2\upsilon)} \quad (5)$$

where $\boldsymbol{\sigma}^{solid}$ is the stress fields, $\boldsymbol{\epsilon}$ is the solid deformation, E is the Young's modulus, υ is the Poisson coefficient and $\mathbf{I}$ is the identity tensor. The coupling equations are modeled by two conditions:
-A kinematic condition given by:

$$\mathbf{u}_f(x,t) = \frac{\partial \mathbf{u}_s}{\partial t} \qquad on \ \ the \ \ blade \quad (6)$$

- A dynamic condition represented by the following equation:

$$\mathbf{n}.\boldsymbol{\sigma}^{solid}_{interface} = \mathbf{n}.\boldsymbol{\sigma}^{fluid}_{interface} \quad (7)$$

Where $\mathbf{n}$ is the unit vector normal to the interface (blade) and $\boldsymbol{\sigma}^{fluid}$ is the stress fields in fluid given by the following equation:

$$\boldsymbol{\sigma}^{fluid} = -pI + \mu_f \nabla \mathbf{u}_f \quad (8)$$

The kinematic condition corresponds to an equality of the fluid and solid velocities resulting in a coordinated mesh movement of the two fields. Thus, when updating the mesh position, the solid displacement velocity will be transmitted to the fluid. The dynamic condition, on the other hand, corresponds to a condition on the fluid forces applied to the solid at the interface.

III. NUMERICAL SIMULATIONS:

The two-way fluid structure interaction analysis couples the transient structural dynamics solver based on the finite element method to the fluid dynamics solver based on the finite volume method. These two domains are coupled by the system coupling interface, which makes the data transfer between the fluid force and the blade displacement. The simulation of this problem is carried out by simultaneous resolution, at each time step, of two independent physical fields of fluid dynamics and structural dynamics and transfer of data between the two fields. For that, it requires a high computational time.

A. Computational Fluid Dynamics Model

The fluid field of the coupled FSI analysis is solved using ANSYS FLUENT solver. The fluid domain is meshed and subdivided into a finite number of control volumes, where the general conservation equations for continuity and momentum are then solved.
The flow domain is composed by a stationary rectangular domain, representing the hydrodynamic flow channel in the CFD model, and a rotating cylindrical domain for modeling the rotation at the rotor angular velocity. The stationary domain has dimensions of 38 cm ($2.16D$) width, 52.8 cm ($3D$) height and 176 cm ($10D$) length. Note that these

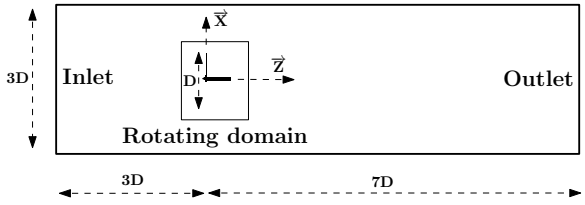

FIG. 1. Dimensions of fluid domains.

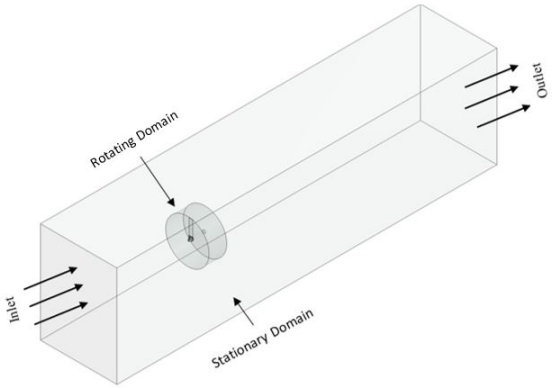

FIG. 2. Computational domain

dimensions are those of the experimental channel of A.S. Eldemerdash and T. Leweke[25]. The cylindrical rotational domain uses a diameter of 27 cm ($1.53D$) and width 50 cm ($2.84D$) to enclose the rotor (blade, hub and shaft). In the previous expressions, D corresponds to the rotor diameter. The domain reference $(x,y,z) = (0,0,0)$ is set at the center of the turbine hub (figure 1). The origin location of the inlet boundary is at a distance of $3D$ from the blade, and the outlet boundary is $7D$ from the rotor center.

TABLE I. Mean blade's tip displacement (blade with pitch angle $\beta = 2.5°$,$\beta = 5°$ and $f = 4Hz$)

Turbulence model	Mean blade's tip displacement [mm]	
	$\beta = 2.5°$	$\beta = 5°$
$k-\omega$	27.5	18.87
$SST\ k-\omega$	27.5	18.86
$k-\varepsilon$	28.8	19.15

Three turbulence models are tested to reach tip Reynolds numbers, Re, as high as 8 10^4 (see below for Re definition): $k-\omega$, $SSTk-\omega$ and $k-\varepsilon$. We checked that these turbulence models give practically the same mean displacements of the blade (table I), and practically the same vortex field in the wake of the rotor blade (see figure 17). Then, as a closure of the unsteady Reynolds-averaged Navier-Stokes equations, we used a standard $k-\varepsilon$ model. The inlet water flow is defined by a constant velocity at $U_0 = 18\ cm/s$ with a turbulence intensity less than 1% . The outlet of the flow channel is defined as a pressure outlet, with a relative pressure of 0 Pa. The wall

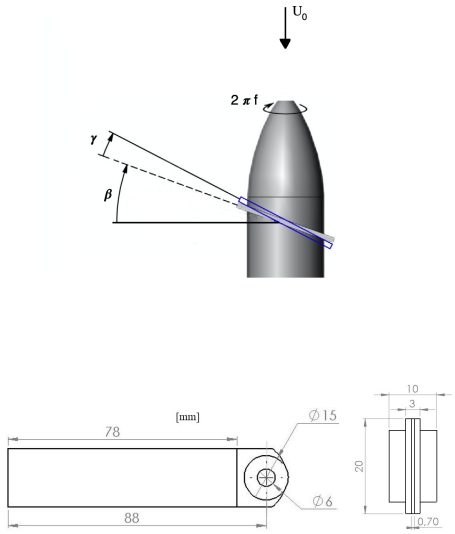

FIG. 3. Rotor, blade and hub's dimensions. Initially, there is no twist (or torsion) γ and β is the pitch angle. The frequency of the rotor is f and the uniform inlet (free stream) velocity is U_0.

boundary condition is defined as no–slip and assigned to different sides of the flow channel as well as to wall-cfd-coupled interface (blade, hub, and shaft). In a no-slip wall boundary condition, the velocity is immediately zero next to the wall.
The rotational domain is characterized by an angular frequency $\omega = 2\pi f$ with f the rotor frequency.

B. Transient structure Model

The main objective of this work is to characterize the deformation of the blade and to study the effect of the aerodynamic parameters on this deformation. We are not interested in the aerodynamic profile of the blade. For this reason, the studied rotor is a moderately flexible rotor in water. It has a simple geometry, consisting of a single rectangular blade of constant thickness, a hub and a shaft. The flexible rotor has a radius $R = 88\ mm$.
The blade is an untwisted rectangular plate of constant chord $c/R = 0.23$. It has a rectangular profile with a constant thickness of 0.7 mm corresponding to 3.5% of the chord. The shaft is an axis with 15 mm (17% of the chord) diameter with an ogive-shaped tip. The various rotor dimensions are summarized in figure 3.

Our objective is to study the elastic behavior of a rotor blade. Then, the blade material used in simulations is the Low-Density Polyethylene (LDPE) with the following fundamental properties: density 1070 kg/m^3, Young's modulus 3.5 GPa, and shear modulus 1.7 GPa. The carbon fiber material is affected to the hub and the nylon material to the shaft.
To identify the inertial forces, we have applied to the rotor a rotational speed with the same value as that of the fluid

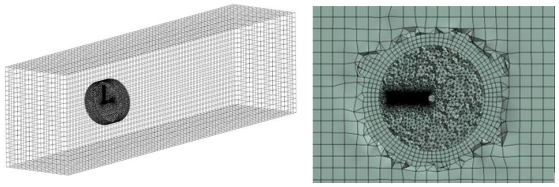

FIG. 4. Grid and sectional view of the computational domain

cylindrical domain. Also, we have identified a fixed distant point at the rotor center to release the moment and the force values. The rotor is fixed at the shaft and the blade faces are defined as coupling interfaces. Due to significant displacements of the blade, we have enabled ANSYS' "large deflection" model to accurately capture its behavior.

C. Coupled Fluid Structure Interaction Model

The coupling between transient structural analysis system and fluid dynamics is provided by the system coupling module of ANSYS Workbench. This module performs coupled simulations with two-way data transfer. In the fluid-solid interface, and due to the pressure and friction forces produced by the fluid, the blade becomes deformed, and this changes the boundaries of the fluid domain. The individual physics of the fluid and structural field are solved separately in their respective domain and then coupled by establishing a data transfer mechanism and passing information across the fluid-solid interfaces.

D. Meshing

The fluid field of the coupled FSI analysis is solved using ANSYS FLUENT solver. The fluid domain is meshed and subdivided into a finite number of control volumes, where the general conservation equations for continuity and momentum are then solved.

The computational domain mesh is realized with "Ansys-Meshing". We have tested several structured and unstructured meshes in order to choose the optimal mesh with which we will have a good result and a computation time not too exaggerated. We reached a good compromise with a mesh having 454188 nodes and, 235001 elements (figure 4).

For a 3D dynamic mesh domain, we cannot apply structured mesh[5,22,26]. For this reason, we applied an unstructured tetrahedron mesh around the blade and more precisely at the level of the rotating domain, while a structured mesh was chosen for the rest of the fluid domain (stationary domain).

To faithfully describe the geometry of the blades, we have refined the mesh around the blade, so we have carried out a mesh with a size of 0.001 m in the vicinity of the coupling interfaces.

A dynamic mesh has been applied to the area near the flexible blade, seat of the fluid structure interaction. We have applied the remeshing, layering and smoothing methods.

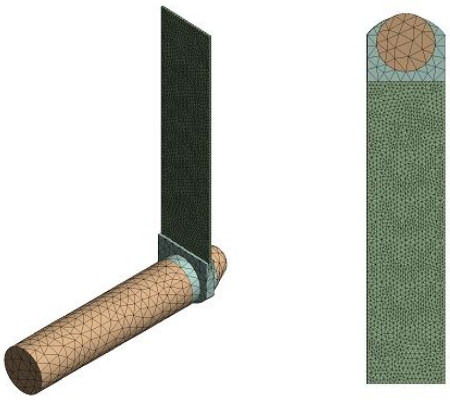

FIG. 5. Structure of the mesh

The structure domain is discretized by an unstructured tetrahedral mesh with 27707 nodes and 13795 elements divided as follows: the element size is 0.001 m in the blade to properly quantify the deformation and 0.003 m at the rotor and the shaft (figure 5).

To test the fidelity and sensitivity of the mesh, we applied a pressure of 100 Pa (as an example) on the upper face of the blade, and we measured the maximum displacement at the tip of the blade. As shown in table II, displacement values for the different element sizes are almost equal. To have the same mesh size as at the fluid-structure interface, we have chosen an element size equal to 0.001 m.

TABLE II. Mesh effect

Element size [m]	Maximum tip displacement [mm]	Relative error [%]
0.003	4.671	–
0.002	4.676	0.11
0.001	4.679	0.06
0.0005	4.680	0.02

IV. RESULTS AND DISCUSSIONS

A. blade deformation

In this section, we study the bending behavior of the rotor blade, and we present the effect of rotational frequency on this type of deformation for a blade pitch angle $\beta = 0^\circ$.

For this study, the free-stream velocity is constant $U_0 = 18cm/s$, and the rotation frequency of the rotor was varied in the range $0 < f < 8Hz$. This corresponds to tip speed ratios $\lambda = 2\pi fR/U_0 = 0-25$, and blade tip Reynolds numbers $Re = 2\pi fRc/\nu = 0-8.8\ \ 10^4$, where ν is the kinematic viscosity of water.

To reduce the time taken by simulations, we are only interested in the short time just after the transient to describe the blade behavior. So we have chosen a total time of simulations equal to 3 *s* (corresponding to more than 6 revolutions of the rotor for the frequency $f = 2\ Hz$). The time step taken in simulations is 1 *ms* for frequencies less than 5 Hz. For the higher frequencies, the time step is decreased to reach the convergence of the data transfer at the coupling level.

We represent, in figure 6, the maximum displacement (in time) and the corresponding stress of the rotor blade with different speeds of rotation for a blade with a pitch angle $\beta = 0^\circ$. For simplifying the presentation, the rotational speed is expressed using the frequency f.
The displacement figures show that the blade deforms in the downstream direction, and the amplitude of the deformation increases with the rotation frequency. For $f = 0\ Hz$, corresponding to a non-rotating rotor, the blade is almost straight with a slightly bent, because of the non-zero free stream.

Figure 7-a presents the evolution of the blade deformation (in the z direction) in time for different rotational frequencies. The deformation undergoes a transient period, then it begins to stabilize around an average value after a number of revolutions. The amplitude of the deformation oscillates according to a period corresponding to the frequency of rotation of the blade.
The variation of the deformation versus time for different positive rotation frequencies (figure 7) shows the increase of the deformation amplitude with frequency for f less than 5. From this value, the amplitude of the deformation begins to decrease.
As a conclusion, the bending of the rotor is not a monotone function with the frequency of rotation.

B. Pitch angle effect

The pitch angle is an important parameter in controlling the performance of wind turbines[27]. We present, in this section, the effect of this parameter on the blade deformation. Figure 8 describes the elastic behavior of the blade. It represents the maximum flapwise deformation of the blade for different pitch angles and different frequencies. The displacement figures, show that the blade deforms in the downstream direction, and the amplitude of the deformation increases with the rotation frequency.

We found that the blade with pitch angle $\beta = 5^\circ$ and $\beta = 10^\circ$, for a higher frequency and for a specific instant, begin to deform in the upstream direction. To properly characterize and study this behavior, we present in figures 9, 10 and 11 the evolution of the blade tip displacement with time for different pitch angles and different speed frequencies. The blade with pitch angle $\beta = 5^\circ$, rotating with $f = 7\ Hz$, begins to deform in the upstream direction after 9 revolutions. The same blade, rotating with $f = 8\ Hz$, deforms in the upstream direction from the 6th revolution (figure 10).

We have found the same behavior for negative frequencies (negative pitch angle), i.e., the deformation increases with rotation frequency except that the amplitude for negative frequencies is greater than that for positive ones (fig 9, 10).

Figure 12 shows the deformation in the z direction for different pitch angles with a rotational frequency $f = 4\ Hz$. It is clear that the amplitude of the deformation decreases with the pitch angle, due to the orientation of the blade with respect to the flow. Indeed, the quadratic bending moment along the z axis increases and the perpendicular surface to the flow decreases.

It is clear from the previous figures that after a transitory, of two or three rotations of the flexible blade, the normalized maximum blade-deformation, z/R, could be written

$$\frac{z}{R} = \frac{\langle z \rangle}{R} + \frac{a}{R}\cos(\omega t + \phi), \tag{9}$$

where $\langle z \rangle$ is the mean bending, a is the amplitude of oscillations, $\omega = 2\pi f$ is the angular frequency of the blade and ϕ is an arbitrary phase. The amplitude increases with frequency, reaches a maximum, then decreases and disappears for high frequencies. When it is maximum, it is of the order $a/R = O(0.1)$. The behavior of $\langle z \rangle / R$ is summed up in figure 13. For the range of parameters considered here, it is clear that (for a fixed pitch) the mean blade deformation increases with frequency, reaches a maximum then decreases with a possibility to change sign for high frequencies. This change of sign is a signature of a transition from downstream to upstream deformation. The frequency corresponding to the maximum is highly dependent on the pitch angle. The upstream bending is obtained for a positive pitch only ($\beta = 5^\circ$) when the frequency is relatively high. Furthermore, at a given frequency, there is no reflection symmetry of the mean blade deformation (with respect to $\beta = 0$ when the sign of the pitch is changed), even for low frequencies. finally, it is interesting to note that the maximum of the mean blade deformation is not a monotonic function of the pitch angle.
Figure 14 presents the maximum blade flapwise deformation (taken on the middle line) for different rotation frequencies. The tip positions are all related to a single circle whose center is distant by 2 cm in the radial direction from the rotor center. The initial very slight bent of the blade, for $f = 0Hz$, is due to the non-zero free stream. The maximum blade bending increases with rotation frequency until it reaches its maximum curvature for a specific frequency. Above this frequency, the blade curvature decreases.

To characterize the magnitude of the flapwise deformation, we define θ as the angular position of the blade tip on this circle, with $\theta = 0$ representing the undeformed blade. The variation of this angular position with the rotation frequency f is presented in figure 15 and compared to experimental results. This plot shows clearly the evolution of the amplitude of deformation as a function of the rotation frequency.

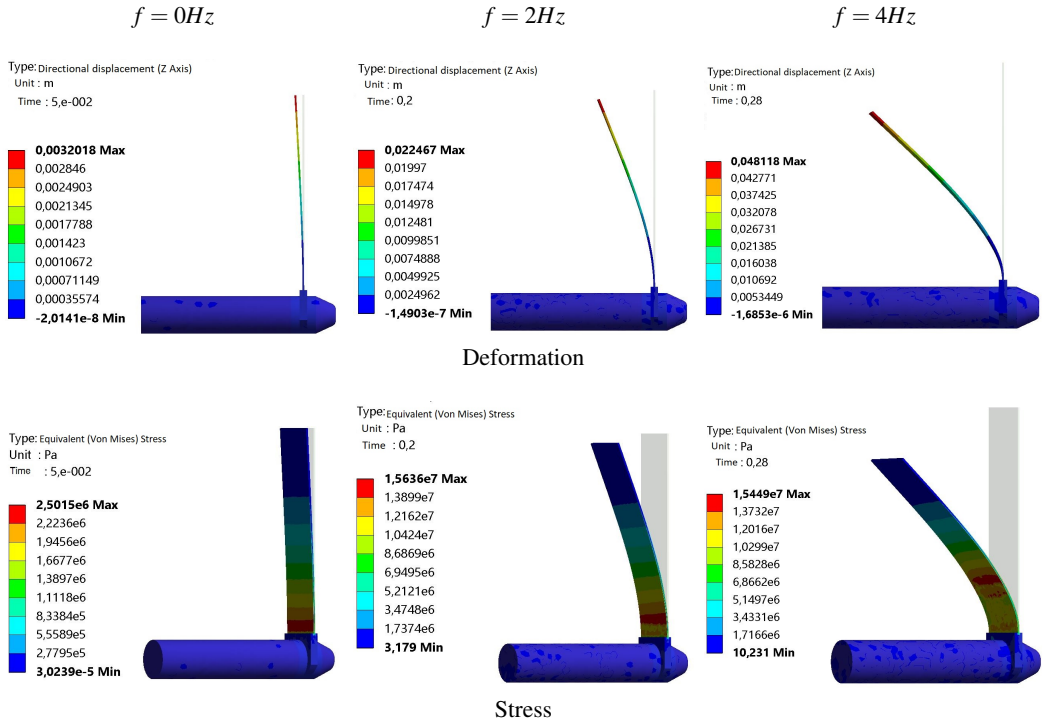

FIG. 6. Maximum flapwise displacement and stress distribution of the blade with $\beta = 0°$, as function of the rotational frequency f.

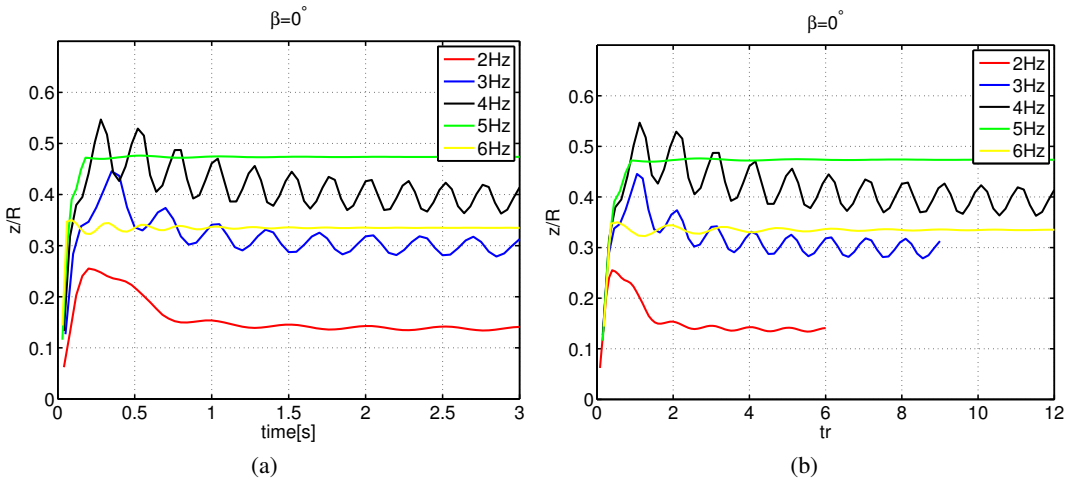

FIG. 7. Total maximum blade deformation variation (a)with time (b)with number of revolution for different frequencies

Figure 15 shows that the experimental and numerical curves have the same shape. Indeed, the amplitude of the deformation increases proportionally to the rotation frequency, then decreases for high frequencies. Moreover, this figure shows that the breaking of symmetry between the negative and positive pitch angles is well captured in our simulations.
The difference in amplitude between numerical simulations and experiments, for high frequencies, can be explained by several reasons. On one hand, in the experimental study, a blade manufactured by 3D printing is used for each frequency of rotation, and as it is known, it is not possible to have the same material properties (e.g. Young's modulus) for parts involving 3D printing. On the other hand, numerically, we cannot reach a high simulation time, so we achieved up to 3 s motion time as indicated above. Then the deformation averages are calculated over a period of 3 s, while for the experiment they are determined over 300 s.

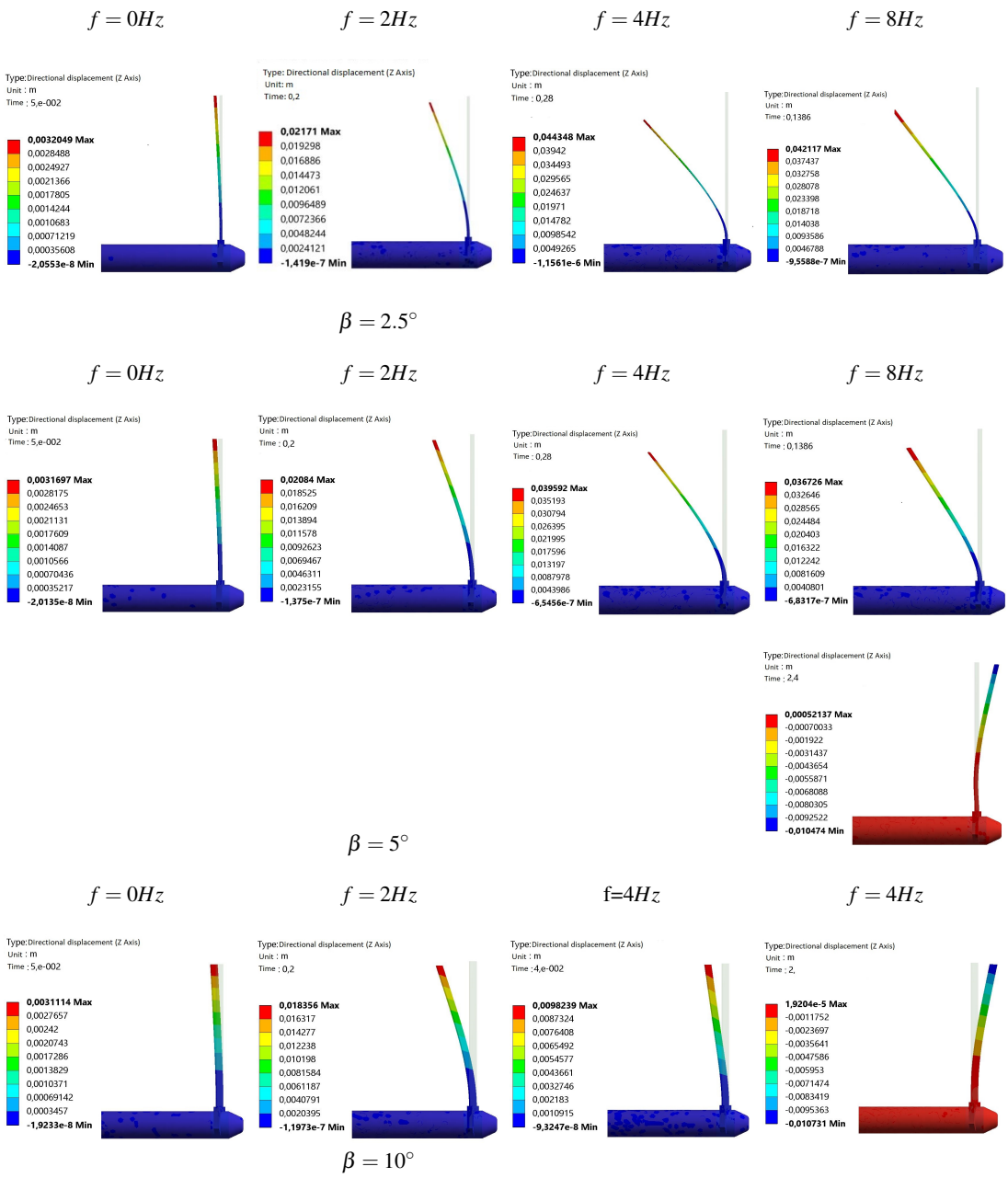

FIG. 8. Maximum flapwise displacement of the blade with $\beta = 2.5°$, $\beta = 5°$ and $\beta = 10°$ as function of rotational frequency f.

C. Torsion

Figure 16 shows the magnitude (in absolute value) of the distribution of the average radial torsion for a blade with a pitch angle of $|\beta| = 2.5°$.
The two figures show clearly that the twist angle increases according to the rotation frequencies, but it is not always maximum at the tip of the blade. For $\beta = 2.5°$, the torsion magnitude reaches a maximum of $1°$ for $f = 3Hz$. For $f = 5Hz$, the magnitude reaches its maximum $\gamma = 0.75°$ at about $1/5$ of the span (from the hub), then it decreases and remains almost stable.
For a negative pitch angle, and in particular for $f = 5Hz$ which presents the highest torsion ($\sim 2.5°$), the twist angle reaches its maximum at 1/5 of the span and remains stable to the end. This maximum twist is explained by the fact that the vortex at the tip is most marked in this configuration (figure 18). This proves that this torsion is influenced by the presence and by the amplitude of the vortex. furthermore, for the negative pitch angle the torsion is a monotone increasing function of the frequency, contrarily the case with a positive pitch.

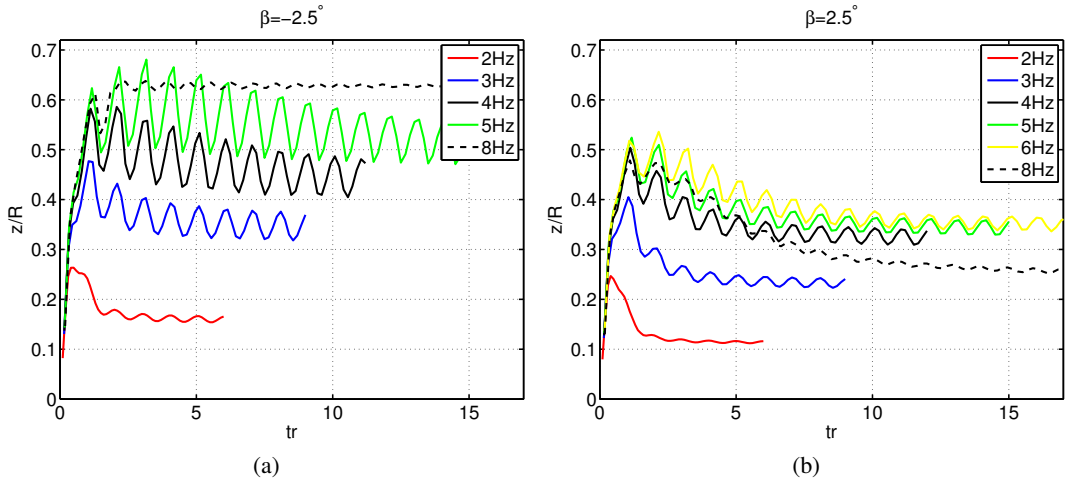

FIG. 9. Total maximum blade deformation variation with number of revolution for different frequencies: (a)$\beta = -2.5^\circ$ (b)$\beta = 2.5^\circ$.

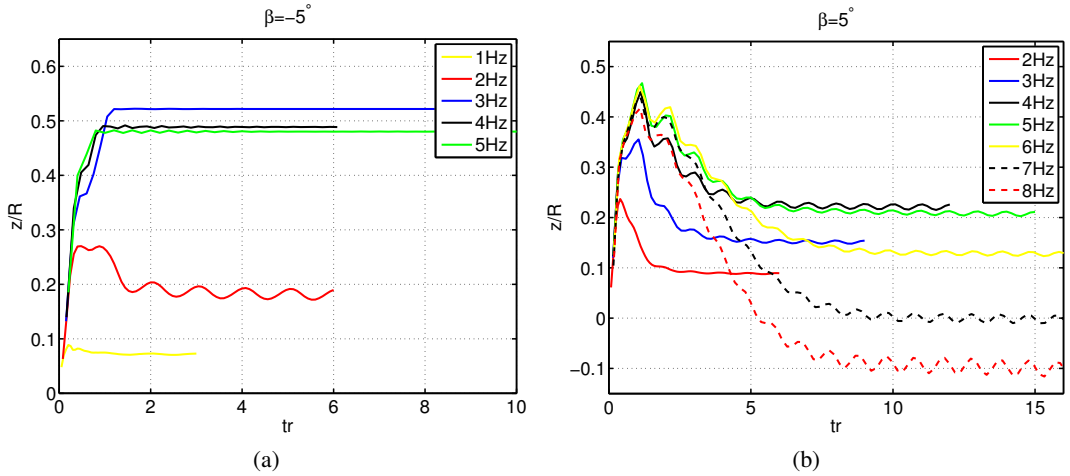

FIG. 10. Total maximum blade deformation variation with number of revolution for different frequencies (a)$\beta = -5^\circ$ (b)$\beta = 5^\circ$.

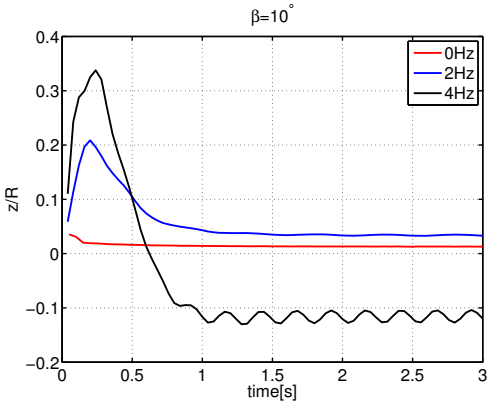

FIG. 11. Total maximum blade deformation variation with time for different frequencies ($\beta = 10^\circ$)

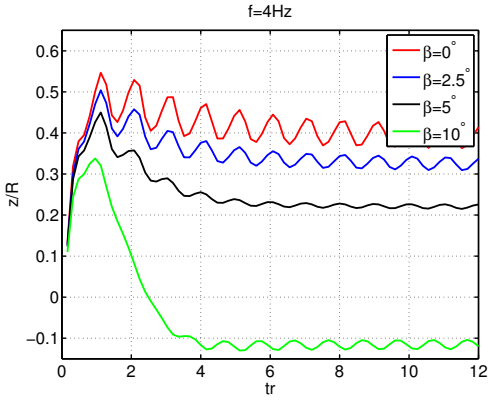

FIG. 12. Blade deformation evolution with time for different pitch angles (f=4 Hz)

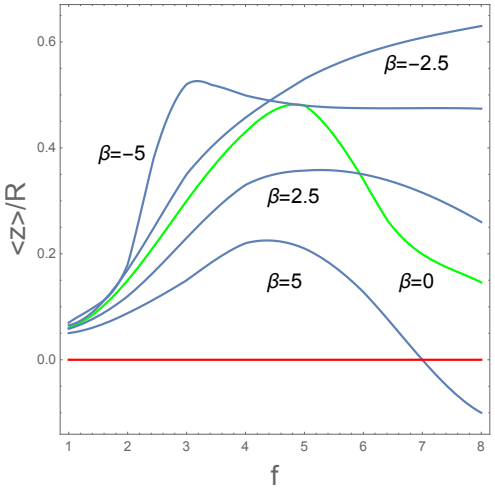

FIG. 13. Normalized mean blade-deformation, $\langle z \rangle / R$, against frequency f (in Hz) for different pitch angles β (in degrees).

D. The flow field in the wake of the rotor

This section presents the study of the time-averaged and phase-averaged vorticity field for pitch angles of $\beta = \pm 2.5°$. Phase-averaged means that images are taken at the same phase of the rotor rotation, i.e. when the rotor comes back to the same position. The average of these images is presented.
In this part, we are only interested in the vortex near the blade. Figure 18 shows that for a positive pitch angle, the vortex wake extends radially and in the flow direction. In the case where the pitch angle is negative, the rotor has a concentrated flow area around the blade, which stays restricted around this blade for frequencies $\gtrsim 4Hz$. This phenomenon is called the "Vortex Ring State" VRS. In fact, this phenomenon is unstable: the vortex ring is discharged in the wake at low frequencies (compared to the frequency of the rotor), which causes strong variations of the fluid forces acting on the blades[28]. This phenomenon resembles the flow structure of the turbulent ring state of a helicopter, which is a dangerous condition that causes its descent. Figure 18 shows also the vortex field in the wake of the rotor for a rigid rotor in the same conditions. No VRS is observed for the rigid rotor. It can be concluded that the flexible structure, with a negative pitch in the present study, is in favor of the VRS which appears for particular frequencies that are to be avoided.

Finally, it is interesting to note that the tip vortex changes sign with that of the blade deflection. This can be seen in figure 19. Note that this change of sign is in agreement with experimental results of Eldemerdash and Leweke[25].

V. CONCLUSIONS

We have studied, for the first time, the mean deflection evolution of a flexible rotor blade using a coupled model based on Navier-Stokes equations, for the fluid flow, and linear elasticity equations for the blade deformation. Turbulence effects are also included in the present study. We have characterized the deformation of this moderately flexible rotor, considered as working in water. We used two nondimensional control parameters in the present study, namely, the tip Reynolds number and the tip speed ratio (related to the frequency of rotation and to the free stream velocity). We also considered positive as well as negative pitches. We show that the blade deformation is highly dependent on the rotation frequency, the pitch and its sign. The mean and maximum deformations of the blade tip increase as a function of the rotation frequencies. At a critical frequency, this deflection starts to reduce. Typically, the blade deflects in the downstream direction, but for particular configurations of pitch angle and rotation frequency, the blade starts to deflect in the upstream direction from a given time. We computed the torsion of the blade, along the span, and show its dependence on the frequency and the pitch.
Understanding the deformations and the elastic behavior of the blade helps us to properly study and characterize its vortex wake. We find that for a negative pitch, there is a critical frequency above which a Vortex Ring State (VRS) is present. Under the same conditions, no VRS is observed for a rigid rotor. Elasticity enhances the possibility for the appearance of the dangerous (for some applications) VRS.

The present results, particularly those in figures 13 and 16, could be used to validate coupled models based on the interaction between a flexible rotor and a model of its wake represented with a helical vortex. Such coupled models are actually under active developments[29].

[1] X. Zhang, Z. Wang, and W. Li, "Structural optimization of h-type VAWT blade under fluid-structure interaction conditions," Journal of Vibroengineering **23**, 1207–1218 (2021).
[2] M. Ali and M. Abid, "Self-similar behaviour of a rotor wake vortex core," Journal of Fluid Mechanics **740**, R1 (2014).
[3] K. Lee, Z. Huque, R. Kommalapati, and S.-E. Han, "The evaluation of aerodynamic interaction of wind blade using fluid structure interaction method," Journal of Clean Energy Technologies **3**, 270–275 (2015).
[4] K. Lee, Z. Huque, R. Kommalapati, and S.-E. Han, "Fluid-structure interaction analysis of nrel phase vi wind turbine: Aerodynamic force evaluation and structural analysis using fsi analysis," Renewable Energy **113**, 512–531 (2017).
[5] L. Wang, R. Quant, and A. Kolios, "Fluid structure interaction modelling of horizontal-axis wind turbine blades based on cfd and fea," Journal of Wind Engineering and Industrial Aerodynamics **158**, 11–25 (2016).
[6] H. Kim, S. Lee, E. Son, S. Lee, and S. Lee, "Aerodynamic noise analysis of large horizontal axis wind turbines considering fluid–structure interaction," Renewable Energy **42**, 46–53 (2012).
[7] L.-W. Chen, C.-Y. Xu, and X.-Y. Lu, "Numerical investigation of the compressible flow past an aerofoil," Journal of Fluid Mechanics **643**, 97–126 (2010).
[8] M. A. Hossain, Z. Huque, R. R. Kammalapati, and S. Khan, "Numeric investigation of compressible flow over nrel phase vi airfoil," International Journal of Engineering Research and Technology (IJERT) **2**, 1–6 (2013).
[9] C. Song, G. Wu, W. Zhu, and X. Zhang, "Study on aerodynamic characteristics of darrieus vertical axis wind turbines with different airfoil maximum thicknesses through computational fluid dynamics," Arabian Journal for Science and Engineering **45**, 689–698 (2020).
[10] M. T. Bouzaher and B. Guerira, "Impact of flexible blades on the performance of savonius wind turbine," Arabian Journal for Science and Engineering (2022), 10.1007/s13369-022-06631-w.
[11] L. I. Lago, F. L. Ponta, and A. D. Otero, "Analysis of alternative adaptive

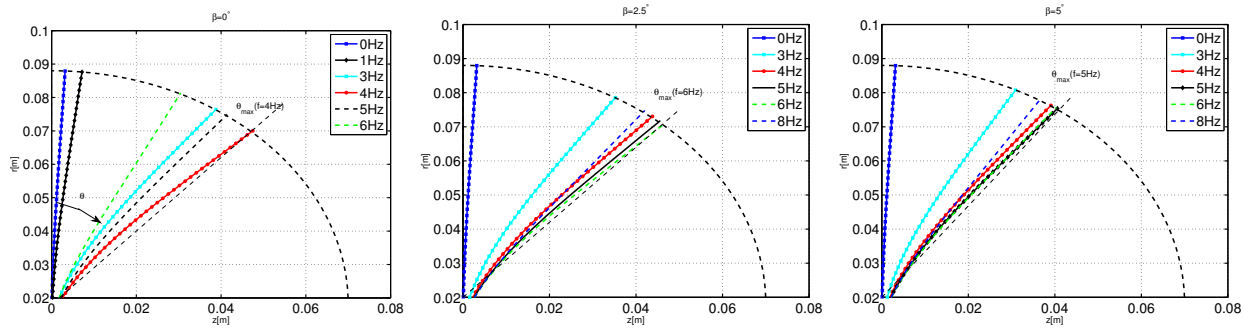

(a) (b) (c)

FIG. 14. Maximum bending deformation of the blade (a) $\beta = 0°$, (b) $\beta = 2.5°$ and (c) $\beta = 5°$.

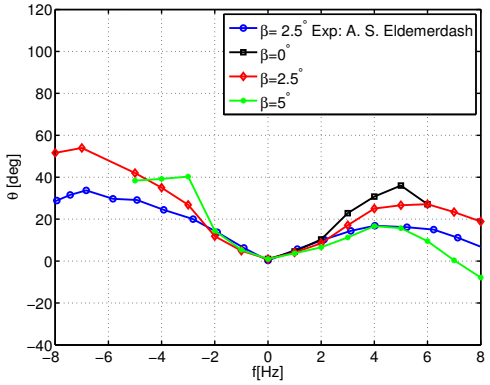

FIG. 15. Amplitude of the tip displacement for three pitch angles ($\beta = 0°$, $\beta = 2.5°$ and $\beta = 5°$)

geometrical configurations for the nrel-5 mw wind turbine blade," Renewable Energy **59**, 13–22 (2013).

[12]M.-S. Jeong, S.-W. Kim, I. Lee, and S.-J. Yoo, "Wake impacts on aerodynamic and aeroelastic behaviors of a horizontal axis wind turbine blade for sheared and turbulent flow conditions," Journal of Fluids and Structures **50**, 66–78 (2014).

[13]B. Mehmet, T. Sergen, T. Mehmet, and S. Besir, "Effect of growth in turbine size on rotor aerodynamic performance of modern commercial large-scale wind turbines," Arabian Journal for Science and Engineering **46**, 7185–7195 (2022).

[14]M. Badshah, S. Badshah, J. VanZwieten, S. Jan, M. Amir, and S. A. Malik, "Coupled fluid-structure interaction modelling of loads variation and fatigue life of a full-scale tidal turbine under the effect of velocity profile," Energies **12** (2019), 10.3390/en12112217.

[15]Y.-B. Chen, Z.-K. Wang, and G.-C. Tsai, "Two-way fluid-structure interaction simulation of a micro horizontal axis wind turbine," International Journal of Engineering and Technology Innovation **5**, 33–44 (2015).

[16]Y. Bazilevs, A. Korobenko, X. Deng, J. Yan, M. Kinzel, and J. O. Dabiri, "Fluid–Structure Interaction Modeling of Vertical-Axis Wind Turbines," Journal of Applied Mechanics **81** (2014), 10.1115/1.4027466.

[17]C. Grinderslev, S. González Horcas, and N. N. Sørensen, "Fluid–structure interaction simulations of a wind turbine rotor in complex flows, validated through field experiments," Wind Energy **24**, 1426–1442 (2021).

[18]L. Wang, X. Liu, and A. Kolios, "State of the art in the aeroelasticity of wind turbine blades: Aeroelastic modelling," Renewable and Sustainable Energy Reviews **64**, 195–210 (2016).

[19]Y. Bazilevs, A. Korobenko, X. Deng, and J. Yan, "Fluid–structure interaction modeling for fatigue-damage prediction in full-scale wind-turbine blades," Journal of Applied Mechanics **83** (2016).

[20]F. Gosselin, E. De Langre, and B. A. Machado-Almeida, "Drag reduction of flexible plates by reconfiguration," Journal of Fluid Mechanics **650**, 319–341 (2010).

[21]E. De Langre, A. Gutierrez, and J. Cossé, "On the scaling of drag reduction by reconfiguration in plants," Comptes Rendus Mécanique **340**, 35–40 (2012).

[22]T. Bano, F. Hegner, M. Heinrich, and R. Schwarze, "Investigation of fluid-structure interaction induced bending for elastic flaps in a cross flow," Applied Sciences **10** (2020), 10.3390/app10186177.

[23]C. S. Bang, Z. A. Rana, L. Könözsy, V. Marchante Rodriguez, and C. Temple, "Numerical investigation and fluid-structure interaction (fsi) analysis on a double-element simplified formula one (f1) composite wing in the presence of ground effect," Fluids **7**, 85 (2022).

[24]V. R. Krishna, S. P. Sanaka, N. Pardhasaradhi, and B. R. Rao, "Hydroelastic computational analysis of a marine propeller using two-way fluid structure interaction," Journal of Ocean Engineering and Science **7**, 280–291 (2022).

[25]A. Eldemerdash and T. Leweke, "Fluid – structure interaction of a flexible rotor in water," Journal of Fluids and Structures **103**, 103259 (2021).

[26]D. R. Sederstrom, *Methods and Implementation of Fluid-Structure Interaction Modeling into an Industry-Accepted Design Tool* , PhD Thesis, University of Denver (2016).

[27]K. Souaissa, M. Ghiss, H. Bentaher, M. Chrigui, and A. Maalej, "Comparative analysis of the performance of small h-darrieus for different pitch control strategies," Proceedings of the Institution of Mechanical Engineers, Part A: Journal of Power and Energy (2022), 10.1177/09576509221113688.

[28]H. Quaranta, *Instabilities in a swirling rotor wake*, PhD Thesis, Aix-Marseille université (2017).

[29]E. Duran Venegas, S. Le Dizès, and C. Eloy, "A strongly-coupled model for flexible rotors," Journal of Fluids and Structures **89**, 219–231 (2019).

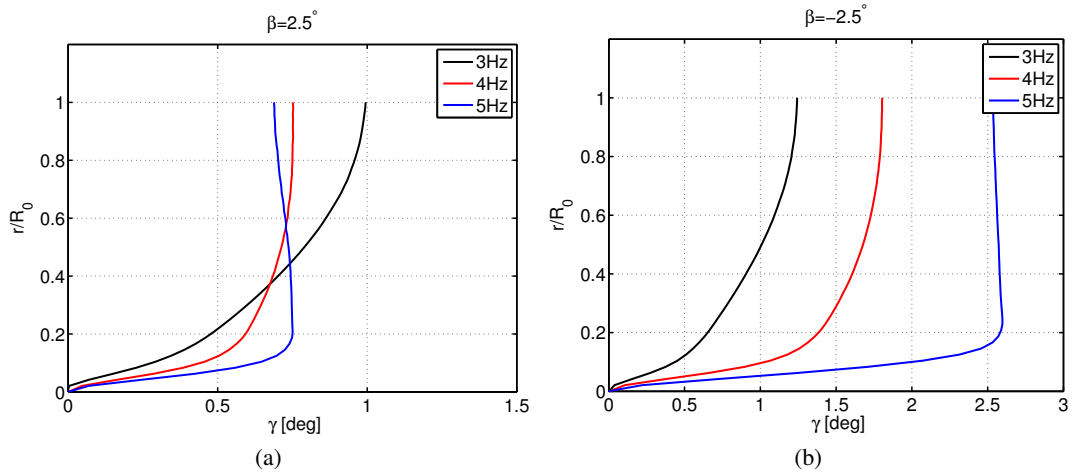

FIG. 16. Twist distributions along the rotor blade for (a) $\beta = 2.5^\circ$ and (b) $\beta = 2.5^\circ$ at various rotation frequencies.

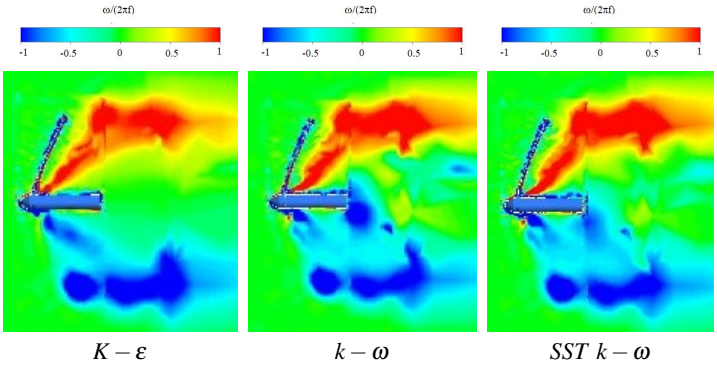

FIG. 17. Averaged azimuthal vorticity in the center plane of the rotor wake for different turbulence models.

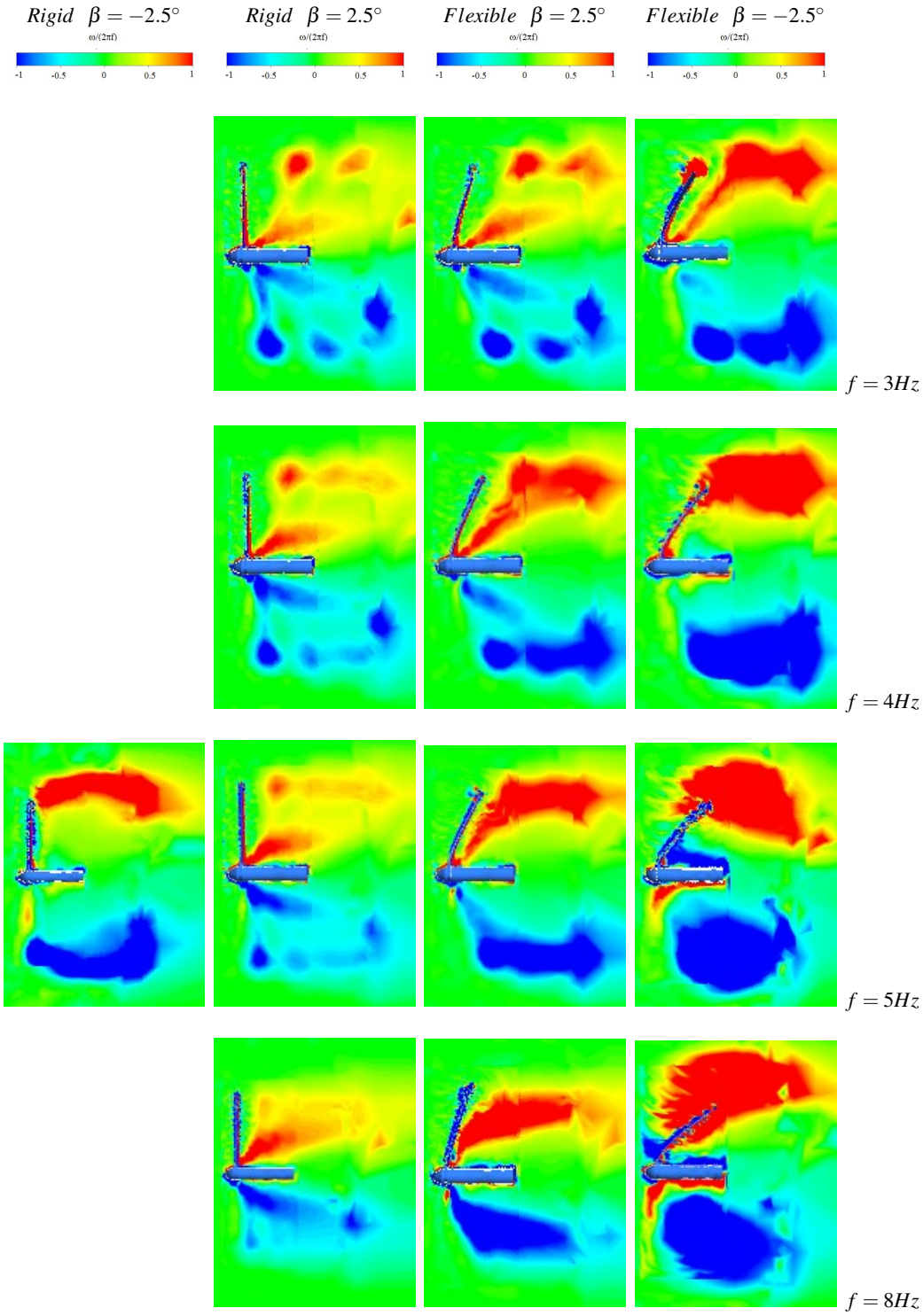

FIG. 18. Averaged azimuthal vorticity in the center plane of the rotor wake for blades with pitch $\beta = \pm 2.5^\circ$ at various rotation rates: for a rigid blade and a flexible blade .

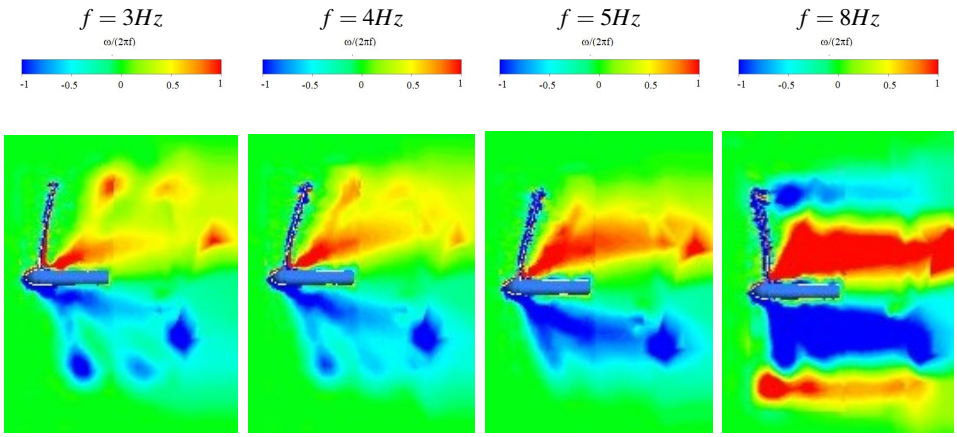

FIG. 19. Averaged azimuthal vorticity in the center plane of the rotor wake for blades with pitch $\beta = 5^\circ$, at various rotation rates.